



HAL
open science

Investigation on the robustness of rotor/stator contact interactions with respect to small mistuning

Florence Nyssen, Alain Batailly

► **To cite this version:**

Florence Nyssen, Alain Batailly. Investigation on the robustness of rotor/stator contact interactions with respect to small mistuning. ASME Turbo Expo 2021, Jun 2021, Virtual, United States. hal-03286203

HAL Id: hal-03286203

<https://hal.science/hal-03286203v1>

Submitted on 13 Jul 2021

HAL is a multi-disciplinary open access archive for the deposit and dissemination of scientific research documents, whether they are published or not. The documents may come from teaching and research institutions in France or abroad, or from public or private research centers.

L'archive ouverte pluridisciplinaire **HAL**, est destinée au dépôt et à la diffusion de documents scientifiques de niveau recherche, publiés ou non, émanant des établissements d'enseignement et de recherche français ou étrangers, des laboratoires publics ou privés.

Investigation on the robustness of rotor/stator contact interactions with respect to small mistuning

Nyssen F., Batailly A.¹

Abstract

In this work, the impact of small mistuning on rotor/stator contact interactions is investigated. First, a detailed study of a rotor/stator interaction between the first bending modes and the second engine order is presented in the tuned case. Then, a numerical investigation on the effect of mistuning on the studied rotor/stator contact interaction is carried out. In particular, a stochastic analysis is performed to evaluate the robustness of the interaction with respect to the mistuning level. Simulations are conducted using a reduced order model (ROM) of an industrial bladed disk that combines both physical degrees of freedom (along blades tip for contact treatment) and modal coordinates. Mistuning is introduced in the tuned ROM by means of a modified version of the component mode mistuning method that allows to keep physical degrees of freedom within the reduced basis. Nonlinear amplification factors, i.e. the amplification factors in the context of contact nonlinearities, are compared with their linear counterparts, the latter are computed using a linear forcing on each blade using a two nodal diameters traveling wave excitation on the mistuned and the tuned bladed disk. The comparison between the linear and nonlinear amplification factor for each sample highlights that no correlation exists between a mistuning pattern leading to high amplifications in a linear context or when contact nonlinearities are taken into account. Therefore, dedicated analyses on the effect of mistuning should be undertaken with contact nonlinearities considerations at the design stage especially if intentional mistuning is considered.

Keywords

rotor/stator interaction; mistuning; multi-sector bladed disk

¹ - Department of Mechanical Engineering, École Polytechnique de Montréal, P.O. Box 6079, Succ. Centre-Ville, Montréal, Québec, Canada H3C 3A7

Enquête sur la robustesse des interactions rotor/stator au désaccordage faible

Nyssen F., Batailly A.¹

Résumé

Dans ce travail, l'impact du désaccordage faible sur les interactions rotor/stator est étudié. Tout d'abord, une étude détaillée d'une interaction rotor/stator entre les premiers modes de flexion et le deuxième régime moteur est présentée dans le cas accordé. Ensuite, une étude numérique de l'effet du désaccordage sur l'interaction rotor/stator étudiée est effectuée. En particulier, une analyse stochastique est effectuée pour évaluer la robustesse de l'interaction par rapport au niveau de désaccordage. Les simulations sont menées en utilisant un modèle réduit d'un disque aubagé industriel qui combine des degrés de libertés physiques (le long du sommet d'aube pour le traitement du contact) et des coordonnées modales. Le désaccordage est introduit dans le modèle réduit accordé au moyen d'une version modifiée de la méthode "component mode mistuning" (CMM) qui permet de retenir des degrés de libertés physiques dans la base réduite. Les facteurs d'amplification nonlinéaires, i.e. les facteurs d'amplification dans le contexte de nonlinéarités de contact, sont comparés avec leurs homologues linéaires, ces-derniers étant calculés en utilisant un forçage linéaire sur chaque aube selon une excitation tournante à deux diamètres nodaux sur le disque aubagé désaccordé et accordé. La comparaison des facteurs d'amplification linéaires et nonlinéaires pour chaque échantillon met en évidence qu'aucune corrélation n'existe entre un motif de désaccordage menant à une forte amplification dans un contexte linéaire ou quand les nonlinéarités de contact sont prises en compte. Par conséquent, des analyses dédiées à l'effet du désaccordage doivent être menées avec nonlinéarités de contact dès l'étape de conception, en particulier si un désaccordage intentionnel est considéré.

Mots-clés

interactions rotor/stator; désaccordage; disque aubagé multi-secteurs

1 - Département de génie mécanique, École Polytechnique de Montréal, P.O. Box 6079, Succ. Centre-Ville, Montréal, Québec, Canada H3C 3A7

INTRODUCTION

In turbomachinery, the unavoidable small discrepancies between each blade stemming from manufacturing tolerances or material non-uniformities, known as *mistuning*, have a strong impact on the dynamics of bladed disks. Over the past decades, numerous research works have been carried out focusing on the effect of mistuning on the bladed disks dynamics in a linear context [1, 2]. The main consequences of mistuning are the frequency splitting [3], the localization of the vibration energy within a few blades [4, 5] and the amplification of the maximum blade response that may lead to high cycle fatigue [6, 7]. With the increasing occurrence of nonlinear interfaces (such as frictional contacts at the blade root or between shrouds) within the engines, researchers have recently investigated the coupled effect of mistuning and nonlinear phenomena [8, 9, 10, 11, 12, 13, 14].

In this work, the focus is on the impact of small mistuning on rotor/stator contact interactions. Indeed, to lower aircraft engines consumption and to comply with always more restrictive environmental requirements, clearances between the rotating and stationary components within the engines are reduced to decrease aerodynamic losses, this may also lead to occurrences of rotor/stator contact events. The vast majority of studies on rotor/stator interactions have been conducted considering a single blade [15]. First investigations on full bladed disk dynamics have been carried out using a two-dimensional phenomenological model in both tuned and mistuned configurations [16]. On this academic model, a higher amplification of the vibration amplitudes has been evidenced in a nonlinear context compared to linear forced responses. In this work, a full industrial bladed disk is considered. Following an in-depth analysis of a specific tuned rotor/stator interaction, the effect of mistuning on these interaction is assessed. The aim is to analyze the robustness of the rotor/stator contact interaction with respect to the mistuning level using Monte Carlo simulations. To handle industrial finite element models in the stochastic analysis, reduction techniques are mandatory to decrease the model size and accelerate computation times. Simulations are conducted using a reduced order model (ROM) that takes advantage of its cyclic symmetry property and that combines both physical degrees of freedom (along blades tip for contact treatment) and modal coordinates. As a first step towards a more comprehensive understanding of the influence of mistuning on blade-tip/casing contact interactions, centrifugal and thermal effects are neglected in this study. An explicit central finite difference time integration procedure coupled with Lagrange multipliers is used to solve the equations of motion at each time step [17]. The abradable layer, a sacrificial material deposited on the casing inner surface to reduce contacts severity, is modeled using radial elasto-plastic rod elements distributed along the casing circumference [18].

In the second section of the article, the rotor/stator interaction between the first bending modes and the second engine order is detailed for an industrial bladed disk considering a tuned configuration. In particular, the radial displacement at the tip of each blade as well as the wear profile are analyzed in the vicinity of the interaction angular speed. In the third section, the developed methodology to build the mistuned reduced order model is presented. Mistuning is introduced in the ROM by means of a modified version of the component mode mistuning method. This allows to retain physical degrees of freedom along the blade-tip within the reduced basis in order to handle contact constraints directly within the reduced space. A small proportional mistuning located on the blades is assumed. In the fourth section, a stochastic analysis is carried out to evaluate the robustness of the interaction with respect to the mistuning level. Simulations are conducted for different mistuning levels, with 1000 samples for each level. The nonlinear amplification factor, *i.e.* the amplification factor in the context of contact nonlinearities, is defined as the ratio between the maximum radial displacement of all blades boundary nodes in the mistuned case and in the tuned case. The obtained nonlinear amplification factors are compared with their linear counterparts: the linear amplification factor is computed using a linear forcing on each blade using a two nodal diameters travelling wave excitation on the mistuned and the tuned bladed disk. For the sake of confidentiality, all frequencies, angular speeds and displacement amplitudes are normalized.

TUNED BLADE/CASING CONTACT INTERACTION

Industrial bladed disk model

The finite element model of the reference sector of the studied industrial bladed disk is shown in Fig. 1. The blade is colored in light gray, the disk in dark gray, and the cyclic boundary nodes are highlighted in orange. The full bladed disk counts 21 sectors. The bladed disk nominal angular speed is denoted Ω_n . The structure is clamped at

its downstream flange. A reduced order model (ROM) is built based on an extension of the Craig-Bampton method in the Fourier basis to take advantage of the cyclic symmetry of the structure [19]. Both physical and modal degrees of freedom are included in the ROM: five boundary nodes (see black dots in Fig. 1) are retained on each blade along their tip, from the leading edge (LE) to the trailing edge (TE), and 20 modes per harmonic are included.

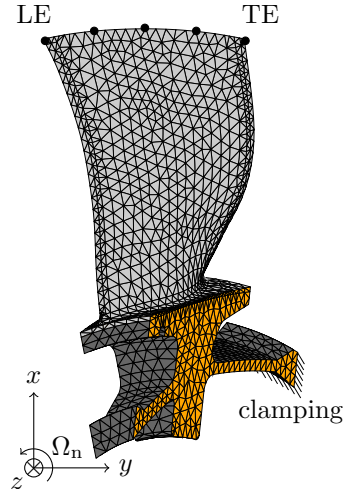


Figure 1. FINITE ELEMENT MODEL OF THE REFERENCE SECTOR OF THE BLADE DISK: BLADE (■), DISK (■), BOUNDARY NODES (●) AND CYCLIC BOUNDARY NODES (■).

The Campbell diagram of the studied bladed disk is presented in Fig. 2. The focus is made on the interaction between the first bending (1B) modes and the engine order (EO) 2. The angular speed Ω_i corresponds to the crossing between the engine order 2 and the first bending mode with 2 nodal diameters. The angular speed range of interest $[\Omega_1, \Omega_2]$ highlighted in orange is centered around Ω_i . All angular speeds in the interval $[\Omega_1, \Omega_2]$ are lower than the nominal engine angular speed Ω_n , which implies that these angular speeds are passed through during a limited number of engine revolutions to reach the nominal angular speed.

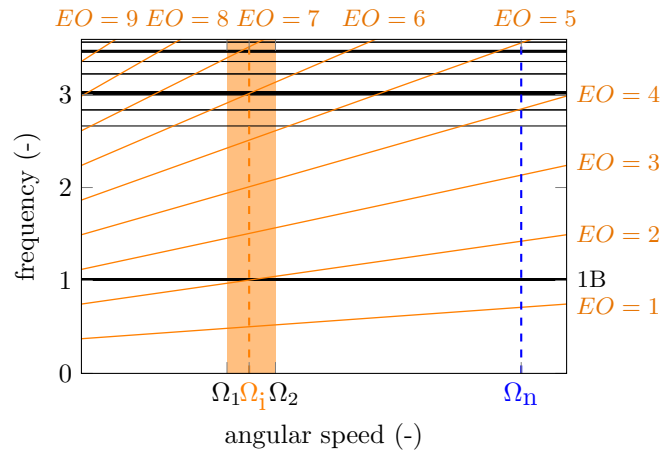


Figure 2. CAMPBELL DIAGRAM.

Definition of the contact scenario

Contact simulations are carried out using an explicit central finite difference time integration scheme to solve the equation of motion. A constant time step of 10^{-6} s is used. Simulations are conducted on 100 engine revolutions at constant angular speed, for 1500 different angular speeds. Among them, 76 are in the range of interest $[\Omega_1, \Omega_2]$. The surrounding casing is assumed to be rigid with an initial blades/casing clearance identical for all boundary nodes to prevent any initial blades/casing interpenetration. During the first 0.04 s of the simulation, the casing is progressively deformed at two opposite angular locations such that contacts are initiated and occur preferentially at these two lobes of deformation. Such deformation is assumed to be consistent with the influence of a thermal load on the casing and leads to contact initiation [20]. No forcing and no initial deformation are applied on the blade airfoils. The abradable layer deposited along the casing circumference is modeled as elasto-plastic radial rod elements, their plastic deformation following contacts representing the wear [18]. The maximum radial displacement

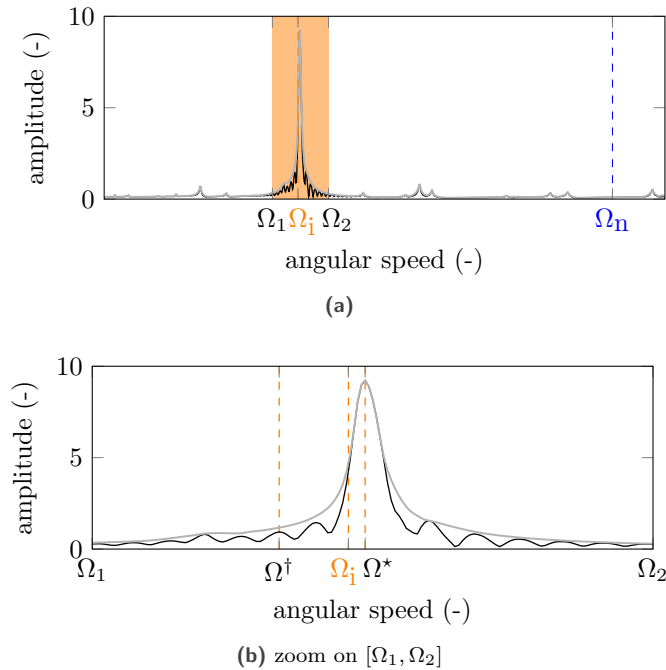


Figure 3. MAXIMUM RADIAL DISPLACEMENT FOR ALL REVOLUTIONS (—), AND FOR THE LAST REVOLUTION (---).

among all boundary nodes at each angular speed is plotted in Fig. 3a, with a zoom on the angular speed range $[\Omega_1, \Omega_2]$ in Fig. 3b. Though the investigated phenomenon is inherently nonlinear due to contact occurrences, one may note that the interaction speed Ω^* is only a few percents higher the linear prediction Ω_i . This indicates a low level of contact stiffening and a slightly nonlinear system. This softer contact configuration allows to give a first insight on the robustness of contact interactions to mistuning.

The maximum radial displacement is computed on all boundary nodes during the last engine revolution (—) and during the whole simulation (---). The value obtained using the last revolution only is always lower or equal to the one computed for the all simulation. A lower value considering only the last revolution means that the maximum of amplitude occurs during the transient response, while the signal reaches a steady state at a lower amplitude. As an example, the radial displacement at the leading edge of blade 1 for the angular speed Ω^\dagger is computed for 1000 engine revolutions for visualization purposes and plotted in Fig. 4a. In the current study, the first 100 revolutions only (in black) are simulated. The transient response effectively leads to higher vibration amplitudes than the stationary response starting after 750 revolutions. Also, depending on the angular speed, the 100th revolution occurs

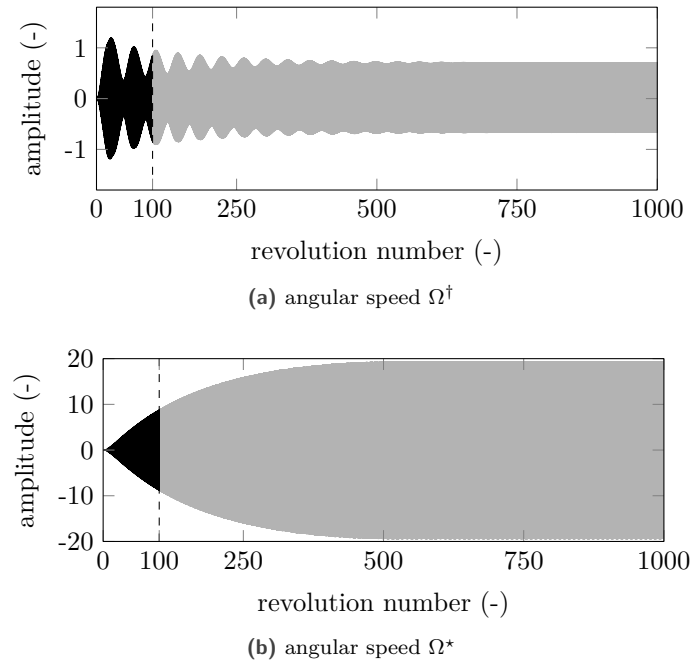


Figure 4. RADIAL DISPLACEMENT AT THE LEADING EDGE OF BLADE 1 FOR 1000 ENGINES REVOLUTIONS.

at a peak or an off-peak in the transient response, which explains the oscillation observed in Fig. 3 for the curve corresponding to the maximum response computed at the 100th revolution. Conversely, the radial displacement at the leading edge of blade 1 for the angular speed Ω^* , for which the maximum radial displacement occurs during the last revolution, is plotted in Fig. 4b for 1000 engine revolutions also. In this case, the amplitude of vibrations always increases until a stationary response has been reached after more than 500 revolutions. But this angular speed corresponds to the interaction with the engine order 2, such that the obtained vibration amplitude already reaches a high value compared to other angular speeds even after 100 revolutions. In the following, only the highest value (*i.e.* the one considered the whole simulation) is retained to be conservative and simulations are conducted over 100 engine revolutions: the considered angular speed range being lower than Ω_n , only a limited number of engines revolutions occur in the angular speed range $[\Omega_1, \Omega_2]$ at the engine ignition. Also, it allows to maintain reasonable computation times for the stochastic analysis of mistuned configurations.

The radial displacement at the leading edge of all blades is depicted in Fig. 5 for the last three revolutions of the simulation at the angular speed Ω^* . The displacement of blade 1 is drawn in black (—). The amplitude of vibration is the same for all blades, with a phase shift of $\frac{2\pi}{N}$ between each blade (with N the total number of sectors). This means that contacts with the abradable layer occur at the same angular locations for all blades. In the rest of this section, results are plotted for blade 1 only.

Abradable wear

The radial displacement of blade 1 (—) at both leading and trailing edges are superimposed to the abradable layer profile (—) in Fig. 6 for the three last revolutions. The abradable profile for the last revolution is underlined in red (—). At the leading edge (Fig. 6a), contacts between the blade and the abradable layer occur between the two lobes induced by the casing deformation. Interpenetrations between the blade and the abradable layer are observed during contact events because of the elastic deformation of the abradable layer. At the trailing edge (Fig. 6b), blade/abradable layer contacts are located just before the two lobes. Interpenetrations also occur due to elastic deformation of the abradable layer.

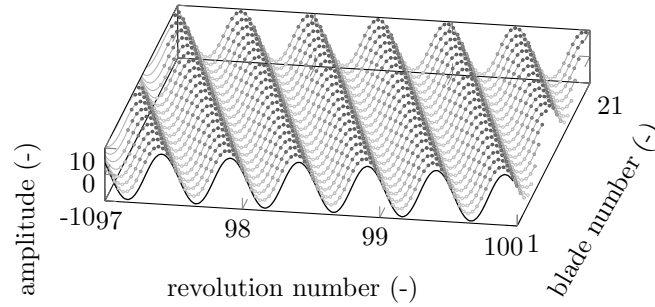


Figure 5. RADIAL DISPLACEMENT AT THE LEADING EDGE OF BLADE 1 (—) AND BLADE 2 TO 21 (—) FOR THE THREE LAST REVOLUTIONS AT THE ANGULAR SPEED Ω^* .

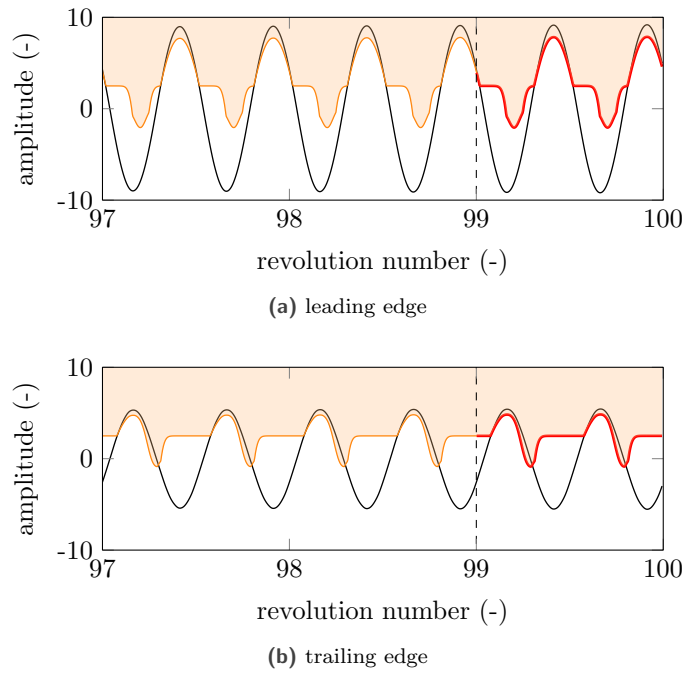


Figure 6. RADIAL DISPLACEMENT (—), ABRADABLE LAYER PROFILE (—) FOR THE THREE LAST REVOLUTIONS, AND ABRADABLE LAYER PROFILE (—) FOR THE LAST REVOLUTION AT THE ANGULAR SPEED Ω^* .

In Fig 7, the time evolution of the blade radial displacement and of the abradable layer profile are drawn in polar coordinates, at both leading and trailing edges for the simulation at the interaction angular speed Ω^* . The displacement curves are colored from white to black as the time increases, while the abradable layer profiles are drawn from white to orange with time. The abradable layer profiles at the end of the simulation are underlined in red (—). At the leading edge (Fig. 7a), at the beginning of the simulation, the blade rotates without any contact. The casing is progressively deformed during the first engine revolutions and the blade impacts the abradable layer at the two lobes (at 90° and 270°). After the contact initiation, a synchronization of the contacts at the angular positions 170° and 350° occurs. At each contact, the abradable layer is worn at these two angular positions at each revolution. At the blade leading edge (Fig. 7b), the blade also starts with a circular motion at the beginning of the simulation. The progressive deformation of the casing along two lobes initiates contacts between the blade and the

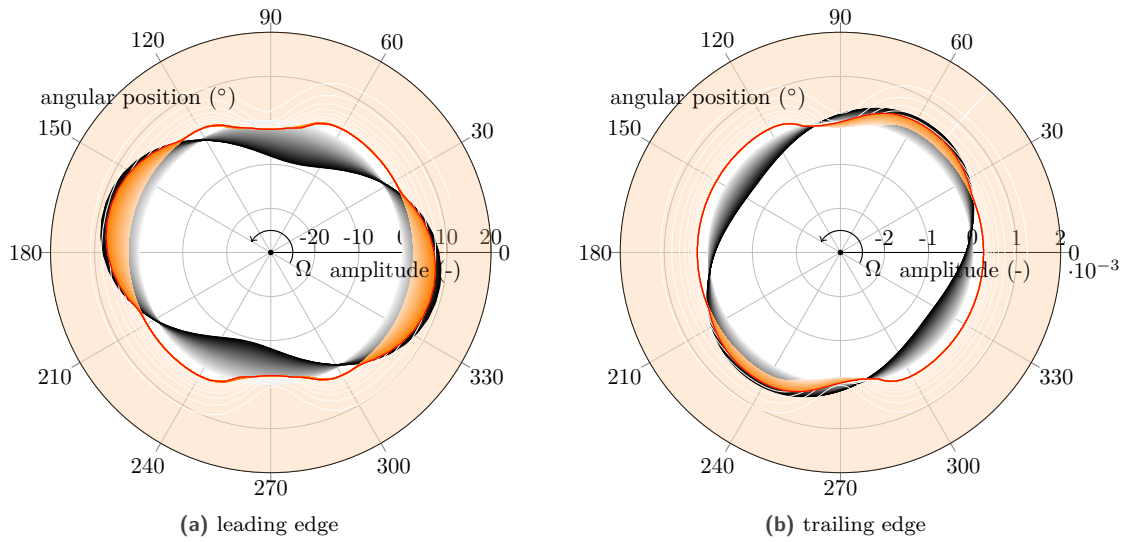


Figure 7. TIME EVOLUTION OF RADIAL DISPLACEMENT (—) AND WEAR PROFILE (—) AT THE ANGULAR SPEED Ω^* , AND ABRADABLE LAYER PROFILE AT THE END OF SIMULATION (—).

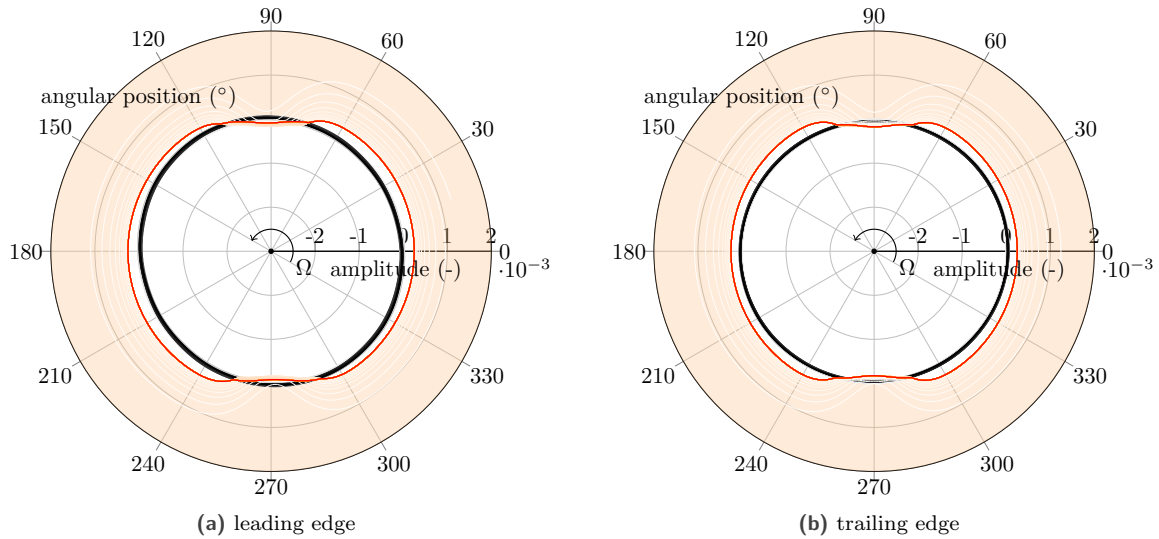


Figure 8. TIME EVOLUTION OF RADIAL DISPLACEMENT (—) AND WEAR PROFILE (—) AT THE ANGULAR SPEED Ω^\dagger , AND ABRADABLE LAYER PROFILE AT THE END OF SIMULATION (—).

abradable layer. A rotation of the two contact areas is rapidly observed as for the blade leading edge, with contacts occurring at the angular positions 55° and 235° . The abradable layer is worn in the vicinity of these two angular positions at each revolution. Even if the abradable layer shows a sophisticated wear profile, only the engine order 2 contributes to the response.

The same quantities are drawn in Fig. 8 for the simulation at the angular speed Ω^\dagger . The behavior of the structure clearly differs from the one obtained at the interaction angular speed Ω^* . At both the leading edge (Fig. 8a) and the

trailing edge (Fig. 8b), the blade rotates without any contact at the beginning of the simulation, and the casing is deformed along two lobes during the first engine revolutions. Contacts occur at these two lobes and the abradable layer is worn. Then, a steady state is achieved, with a contact at the two lobes at each revolution. The amplitudes of vibration and the wear are significantly lower than for the interaction angular speed Ω^* .

Displacement and stress fields

The displacement and stress fields at the time corresponding to the maximum amplitude of displacement of blade 1 for the simulations at the angular speeds Ω^* and Ω^\dagger are shown in Figs. 9 and 10 respectively for the full bladed disk. The used color code goes from white—no displacement and no stress—to red—high displacement or stress. For

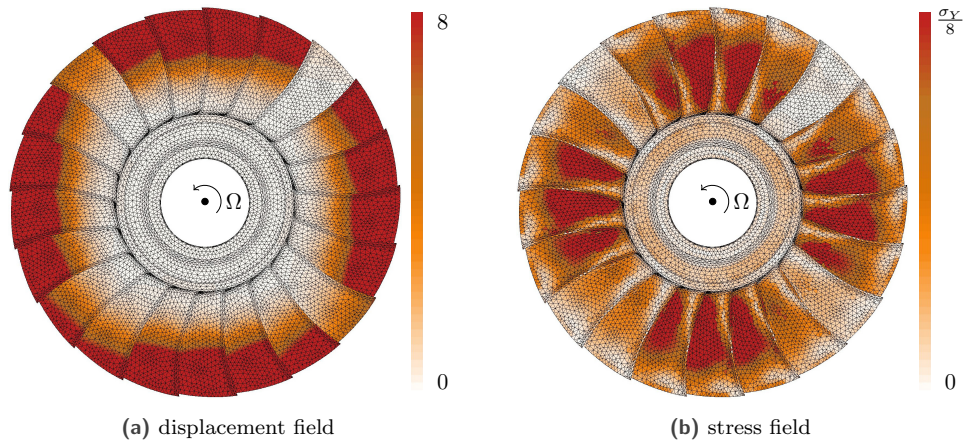


Figure 9. DISPLACEMENT AND STRESS FIELDS AT THE TIME OF THE MAXIMUM DISPLACEMENT OF BLADE 1, AT THE ANGULAR SPEED Ω^* .

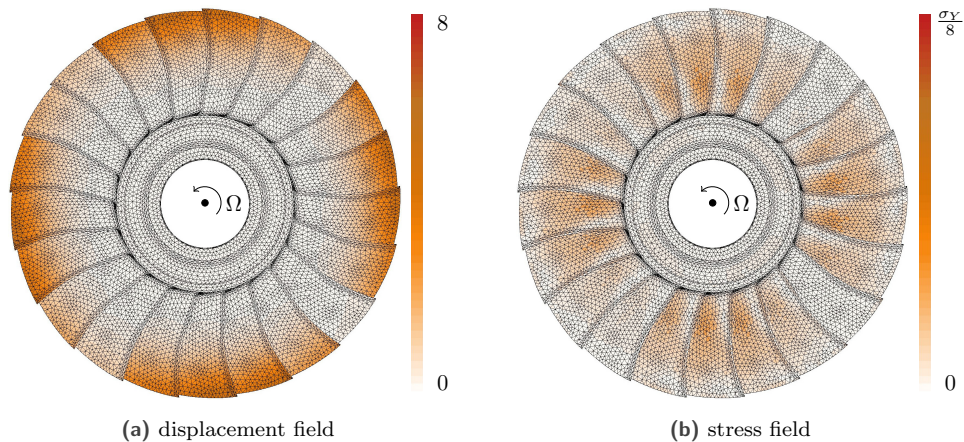


Figure 10. DISPLACEMENT AND STRESS FIELDS AT THE TIME OF THE MAXIMUM DISPLACEMENT OF BLADE 1, AT THE ANGULAR SPEED Ω^\dagger .

both displacement fields, two nodal diameters can be observed on the bladed disk (the odd number of blades renders less distinct the notion of nodal diameters). Indeed, the two lobes initiate a response with two contact areas per

engine revolution. However, the amplitudes of the displacements significantly differ, with a high vibration amplitude for the interaction angular speed and a low amplitude outside of the interaction. For the stress field comparison, the same color scale has been defined, the red color corresponding to $\frac{\sigma_Y}{8}$ with σ_Y the elastic limit of the bladed disk material. The highest stresses are observed in the vicinity of the blades root.

NUMERICAL MODELING OF MISTUNED ROM

The tuned reduced order model of the full bladed disk with N identical sectors is obtained using a component mode synthesis method detailed in [19] based on an extension of the Craig-Bampton method in the Fourier basis as previously mentioned. The stiffness and mass matrices of the ROM are denoted \mathbf{K}_r and \mathbf{M}_r . These matrices combine n_b physical degrees of freedom—associated to nodes along the blade tip retained for the contact treatment—and η modal coordinates. The transformation matrix used to project the structural matrices of the full finite element model to the reduced space is Ψ_r . The eigenfrequencies and eigenvectors of $(\mathbf{K}_r, \mathbf{M}_r)$ are denoted Λ_r and Φ_r respectively.

Mistuning is introduced in the ROM using a modified Component Mode Mistuning (CMM) method [21] for small mistuning that takes into account contact interface degrees of freedom [22], called Component Mode Mistuning with Mixed dof. As in the original CMM method, the structural matrices of the mistuned system are expressed using the modal matrices of the tuned system and the mistuning is modeled as a perturbation in the modal space, using a projection on cantilevered blade modes. The structural matrices of the cantilevered blade are \mathbf{K}_b and \mathbf{M}_b , and the corresponding eigenfrequencies and eigenvectors are denoted Λ_b and Φ_b . Their restriction to R modes, R being called the *restriction parameter*, is written $\Lambda_b|_R$ and $\Phi_b|_R$. The mistuning is assumed to be located on the blades only. Considering a proportional mistuning, the Young's modulus of each blade n ($n = 1, \dots, N$) becomes $E_n = E_0(1 + \delta_n)$, with E_0 the nominal Young's modulus and δ_n the deviation due to mistuning. A deviation of the blade Young's modulus is equivalent to a deviation of its cantilevered eigenfrequencies. Therefore, the mistuned stiffness matrix of blade n in the cantilevered blade modal space writes:

$$\Lambda_n^\delta = \delta_n \Lambda_b|_R \quad (1)$$

The deviation due to mistuning of the stiffness matrix of the full bladed disk in the modal space can be computed using a participation factor \mathbf{Q}_n for each blade n :

$$\Lambda^\delta = \sum_{n=1}^N \mathbf{Q}_n^\top \Lambda_n^\delta \mathbf{Q}_n \quad (2)$$

The participation factor \mathbf{Q}_n can be computed using:

$$\mathbf{Q}_n = (\Lambda_b|_R)^{-1} (\Phi_b|_R)^\top \mathbf{K}_b [\Psi_r \Phi_r]_{N \times R}|_n \quad (3)$$

in which $\Phi_r|_{N \times R}$ stands for the restriction of Φ_r to $N \times R$ modes and $[\cdot]_n$ is the restriction to the degrees of freedom of blade n . The deviation Λ^δ is applied in the modal space (the condition $N \times R \leq n_f + \eta$ must be verified), *i.e.*

$$\boldsymbol{\kappa} = \Lambda_r + \begin{bmatrix} \Lambda^\delta & \mathbf{0} \\ \mathbf{0} & \mathbf{0} \end{bmatrix}, \quad \boldsymbol{\mu} = \mathbf{I} \quad (4)$$

where $(\boldsymbol{\kappa}, \boldsymbol{\mu})$ are the mistuned structural matrices in the modal space. Mistuning is applied on the stiffness matrix only, *i.e.* the mistuned modal mass matrix $\boldsymbol{\mu}$ is equal to the tuned modal mass matrix. Finally, the mistuned matrices can be written in the reduced space using:

$$\mathbf{K}_r^\delta = (\Phi_r^\top)^{-1} \boldsymbol{\kappa} \Phi_r^{-1}, \quad \mathbf{M}_r^\delta = (\Phi_r^\top)^{-1} \boldsymbol{\mu} \Phi_r^{-1} \quad (5)$$

BLADE/CASING INTERACTIONS WITH MISTUNING

The influence of mistuning on the robustness of the interaction between the engine order 2 and the first bending modes is analyzed in this section using the described method. Samples are selected using a random draw with a

uniform distribution ($\delta_n \in [-dE, dE]$), with dE the mistuning level. Three levels of mistuning are considered: 1 %, 2 % and 3 %. Simulations are carried out using the same configuration than for the tuned case, except for the lobes height and initial clearances that are reduced to be closer to operational engine configurations.

Amplification factors

The nonlinear amplification factor (AF) is defined as the ratio between the maximum radial displacement for all boundary nodes in the mistuned configuration and the maximum radial displacement in the tuned case. The convergence of the nonlinear amplification factor with the number of samples is shown in Fig. 11 for the different mistuning levels (percentiles 10 (—), 50 (—) and 90 (—)) as well as the corresponding error. Considering 1000 samples allows to obtain converged values for all percentiles and mistuning levels, the relative error being below 1 %. Therefore, 1000 samples per mistuning levels are considered in the following.

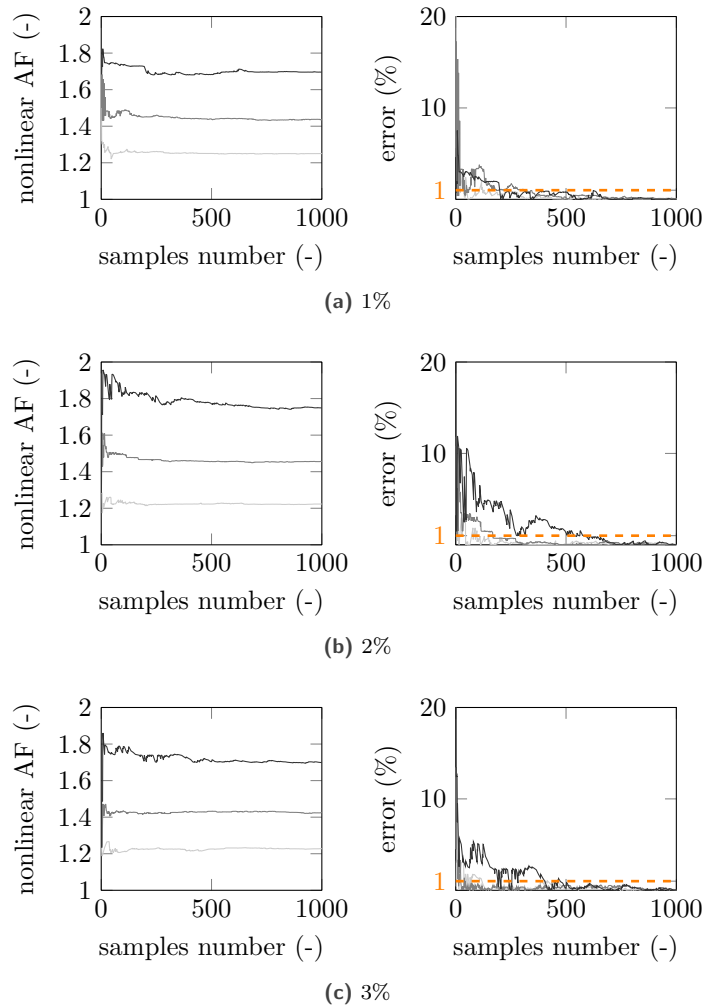


Figure 11. CONVERGENCE OF THE NONLINEAR AMPLIFICATION FACTOR WITH THE NUMBER OF SAMPLES, PERCENTILES 10 (—), 50 (—) AND 90 (—).

The envelop of the maximum responses of all samples over the angular speed range of interest $[\Omega_1, \Omega_2]$ is shown in Fig. 12a for 1 % (■), 2 % (■) and 3 % (■) of mistuning. The tuned response is represented by the black dotted line. The resonance frequency is slightly higher than Ω_1 because of contact stiffening. However, a low stiffening effect is

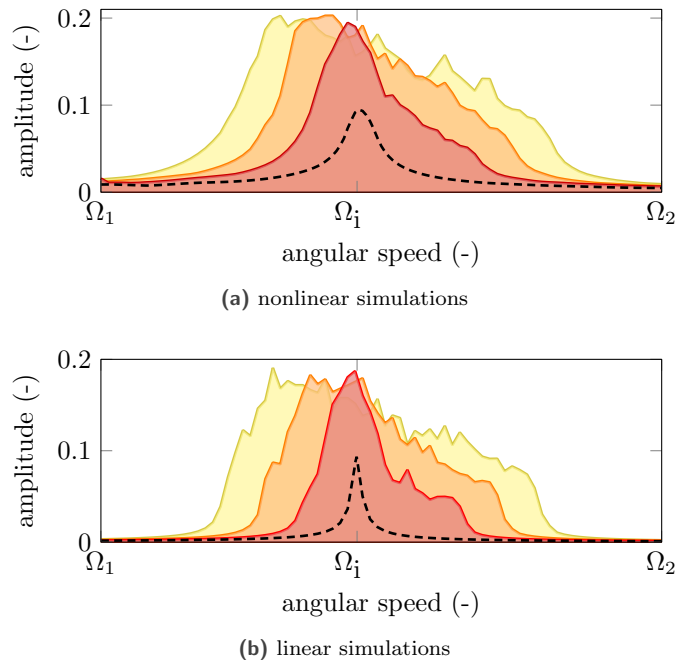


Figure 12. ENVELOP FOR LINEAR AND NONLINEAR SIMULATIONS: TUNED CASE (---), MISTUNING OF 1 % (■), 2 % (■), AND 3 % (■).

observed here, which explained the smooth evolution of the tuned response with respect to the angular speed. For all mistuning levels, a significant increase in the amplitudes is observed compared to the tuned configuration as well as an enlargement of the resonance angular speed range. As the mistuning level increases, the width of the resonance angular speed range increases. The selected angular speed range $[\Omega_1, \Omega_2]$ is large enough to cover the peaks for all samples. No significant change in the maximum amplitude is observed for the different mistuning levels.

The same quantities are drawn in Fig. 12b for linear simulations. Linear simulations consist in a linear forcing with a 2 engine order traveling wave excitation applied at the blades leading edge. The maximum response of the bladed disk in tuned configuration is plotted with a dotted black line. The resonance peak appears at an angular speed equal to Ω_i . For the mistuned cases, the same mistuning patterns than in the nonlinear analysis are considered. The width of the resonance angular speed ranges is lower than in the nonlinear case for all mistuning levels. No significant variation in the maximum amplitude with the mistuning level is observed, as for the nonlinear configuration.

The evolution of the percentiles 10 (—), 50 (—) and 90 (—) of the amplification factors with respect to the mistuning level in both nonlinear (solid lines) and linear (dashed lines) contexts is plotted in Fig. 13. The obtained values are very close, which could be explained by the weak nonlinearity of the studied interaction.

Nonlinear and linear amplification factors are then compared for each of the 1000 samples of each mistuning level in Fig. 14. The density of points is given by the color code from white (low density) to dark color (high density). Even if the percentile values were close (as previously seen in Fig. 13), no correlation is observed between a mistuning pattern that leads to high amplification factor in a nonlinear context and a mistuning pattern that shows a high amplification factor for linear simulations. Therefore, an optimization of the mistuning pattern to reduce the maximum vibration amplitude in a linear context may not lead to an optimal choice when contact nonlinearities are taken into account. For a mistuning level of 1 %, 47.8 % of the samples have a higher nonlinear amplification factor compared to the linear amplification factor. For a mistuning of 2 %, this becomes 48.1 % and for 3 % of mistuning, this is 52.3 % of the samples. Samples are therefore approximately equally spread on both sides of the diagonal line. This observation differs from the conclusions derived from the phenomenological model in [16], for which the

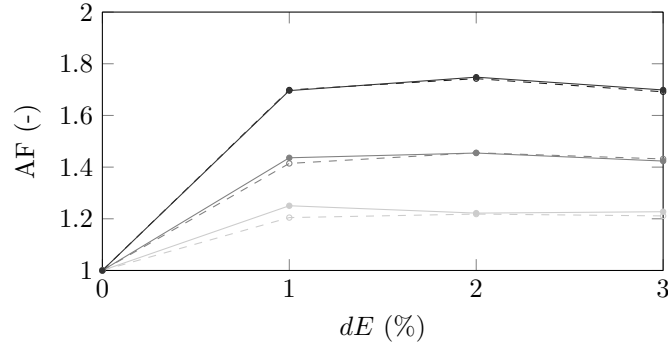


Figure 13. NONLINEAR (—) AND LINEAR (---) AMPLIFICATION FACTORS WITH RESPECT TO THE MISTUNING LEVEL, PERCENTILES 10 (—), 50 (—) AND 90 (—).

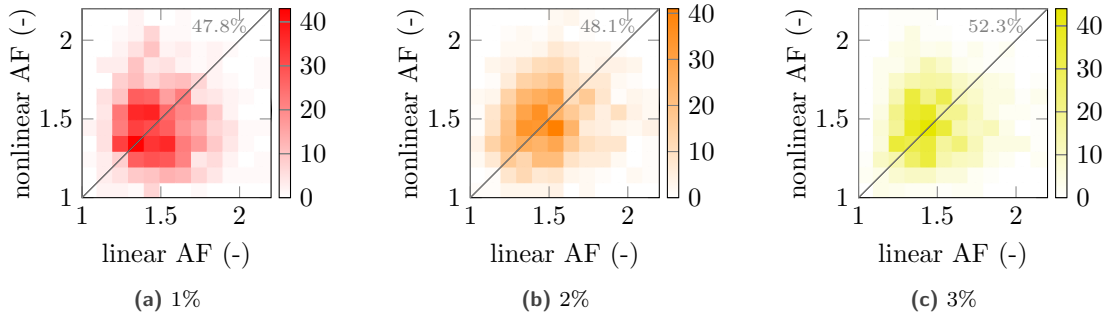


Figure 14. COMPARISON OF THE NONLINEAR AND LINEAR AMPLIFICATION FACTORS.

amplification factors were increased when considering contact nonlinearities. However, the contact stiffening was higher in the case of the phenomenological model (no abradable layer was modeled that softens the blades/casing contacts), which can explain this difference in the behavior.

Localization factors

The localization of the vibrations within the bladed disk is analyzed for both nonlinear and linear simulations. The localization factor (LF) is defined as [23]:

$$LF = 100 \times \frac{\zeta - 1}{\sqrt{N} - 1} \quad \text{with} \quad \zeta = \frac{\max(\mathbf{U}_{\max})}{\sqrt{\langle \mathbf{U}_{\max}^2 \rangle}} \quad (6)$$

in which \mathbf{U}_{\max} is the maximum radial displacement at the blade tips during the last engine revolution, and $\sqrt{\langle \mathbf{U}_{\max}^2 \rangle}$ is the quadratic mean value of \mathbf{U}_{\max} .

The maximum localization factor with respect to the amplification factor is shown in Fig. 15 for the nonlinear case (Fig. 15a) and the linear one (Fig. 15b). Each mistuning level is represented with a different color (1 % (■), 2 % (■) and 3 % (■)). The values for the three selected samples are marked. As the mistuning level increases, the localization factor increases in both nonlinear and linear contexts. A higher localization is obtained for the linear configuration, as well as a lower dispersion of the points. This behavior is however not clearly observed for the amplification factor: no clear impact of the mistuning level stands out. Only a small increase of the maximum amplification factor values is observed as the mistuning level increase. Also, no correlation between the amplification factor and the localization of the vibration is obtained.

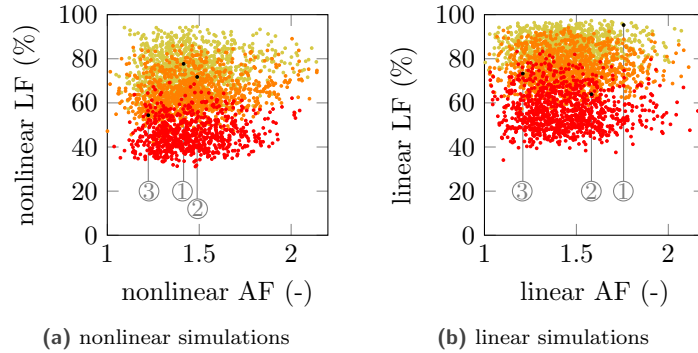


Figure 15. LOCALIZATION FACTORS WITH RESPECT TO AMPLIFICATION FACTORS FOR 1 % (■), 2 % (■), AND 3 % (■) OF MISTUNING.

The comparison of the maximum localization factor over the angular speed range $[\Omega_1, \Omega_2]$ obtained for each sample in a nonlinear and a linear configuration are shown in Fig. 16. As the mistuning level increases, the maximum

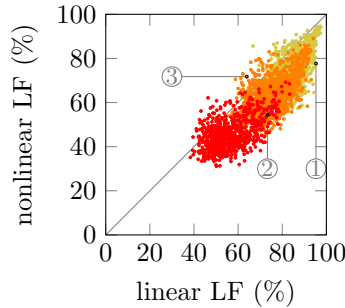


Figure 16. COMPARISON OF THE NONLINEAR AND LINEAR LOCALIZATION FACTORS FOR 1 % (■), 2 % (■), AND 3 % (■) OF MISTUNING.

localization factor increases for both nonlinear and linear cases, as previously noticed. Also, the majority of samples features a higher localization factor in the linear configuration rather than in a nonlinear context. In order to explain this observation, three samples have been selected: samples ① and ② have significantly higher linear localization factors, while sample ③ has conversely a higher nonlinear localization factor (see Fig. 16). The time evolution of the radial displacement at the leading edge of each blade is shown in Fig. 17 for the three selected samples, for nonlinear simulations at the angular speed corresponding to the maximum localization factor. The amplitudes obtained during the last engine revolution are underlined in black, and the relative amplitudes obtained with the corresponding linear simulation (normalized to reach the same maximum amplitude than the nonlinear case) are superimposed in orange for comparison. Also, the amplitude at the last engine revolution in the tuned configuration are drawn in dashed black lines to highlight the response amplification due to mistuning. For sample ① (Fig. 17a), the maximum linear localization factor over $[\Omega_1, \Omega_2]$ is equal to 95.3 %. The vibrations are highly localized to blade 19 (see the orange bars). For the same mistuning pattern and the same angular speed, the displacements in a nonlinear context show that blade 19 also vibrates with a high amplitude compared to the other blades, but an increasing amplitude of vibration is also observed on blade 17. The diverging motion of blade 17 decreases the localization factor (nonlinear LF=68.1 %) since two blades vibrate with a high amplitude. For sample ② (Fig. 17b), the localization factor is again higher in the linear case, with a maximum value of 73.3 %. High amplitudes of vibration are observed for blades 2, 5 and 8 as well as for blades 17, 18 and 19. In a nonlinear context, the relative amplitudes of vibration

differ, in particular blades 2, 5, 8, 17 and 20 demonstrate an increasing amplitude of vibration with time. Again, the localization factor is decreased for the nonlinear case because of the diverging amplitudes of a few blades. Therefore, the analysis of the displacement for these two randomly selected samples allows to explain the lower nonlinear localization factors: the diverging amplitude of different blades leads to a lower localization of the vibrations among the blades. In the case of sample ③ however (Fig. 17c), the nonlinear localization factor, equal to 71.8 %, is higher than its linear counterpart. Blade 7 has the highest amplitude of vibration, and in this case, only blade 7 has a diverging displacement in the nonlinear simulation, which leads to a higher localization factors. Blades 18, 19 and 20 have low responses in the nonlinear case. Therefore, in a few cases (see the few points above the diagonal in Fig. 16), only one blade exhibits a diverging amplitude and higher localization values are obtained.

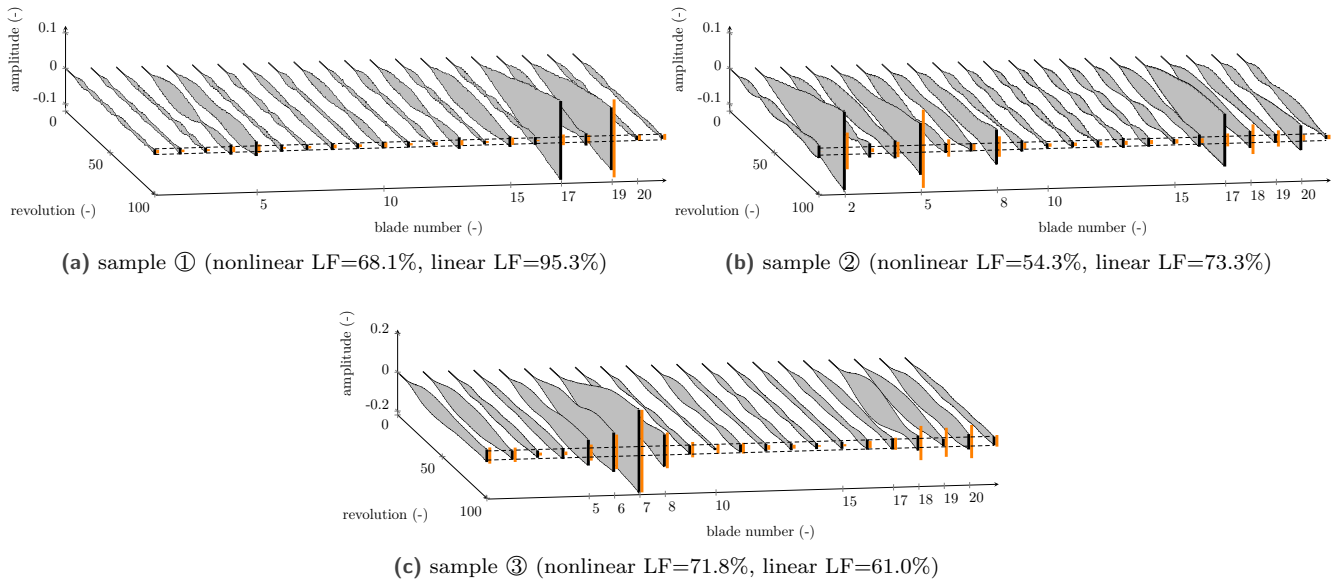


Figure 17. RADIAL DISPLACEMENTS AT THE LEADING EDGE OF EACH BLADE FOR CONTACT SIMULATIONS AFTER 100 REVOLUTIONS (—) AND LINEAR VALUES (—) FOR THE MISTUNED CASE, AND TUNED DISPLACEMENT AMPLITUDE AFTER 100 REVOLUTIONS (---)

The observed diverging amplitudes are directly linked to the transient motion, which occurs during the first engine revolutions (in the tuned case, 750 revolution were necessary to reach a steady state, see Fig. 8). In order to compare the amplitude of vibration of each blade in a steady state configuration, nonlinear simulations are conducted over 1000 revolutions for the three samples at the same angular speed. Results are depicted in Fig. 18, in which the relative linear amplitudes are drawn in orange (the values are normalized with respect to the maximum nonlinear displacement) and the previous results (displacements from revolutions 0 to 100) are colored in black. The corresponding mistuning patterns are superimposed in red (•). For sample ① (Fig. 18a), the amplitude of blade 19 continues to increase during the next revolutions and becomes dominant as in the linear case. The nonlinear localization factor increases (from 68.1% to 89.1%) and the amplitude distribution becomes closer to the linear case. But the amplitude of blade 17 remains higher than in the linear context. For sample ② (Fig. 18b), the nonlinear localization factor increases when considering the steady state (from 54.3% to 60.3%). The highest amplitudes are obtained for blade 2 and 5 as in the linear case. Finally, for sample ③ (Fig. 18c), the steady state results become very close to the linear ones (nonlinear LF=60.5% and linear LF=61.0%). The results obtained for these three samples show that the difference between linear and nonlinear localization factors comes mainly from the choice of considering a fixed number of revolutions (100 in this study), but some differences in the relative amplitude remains even when the steady state is reached due to the transient nonlinear phase. Also, no trend between the mistuning pattern and the blades with high vibration amplitudes can be highlighted.

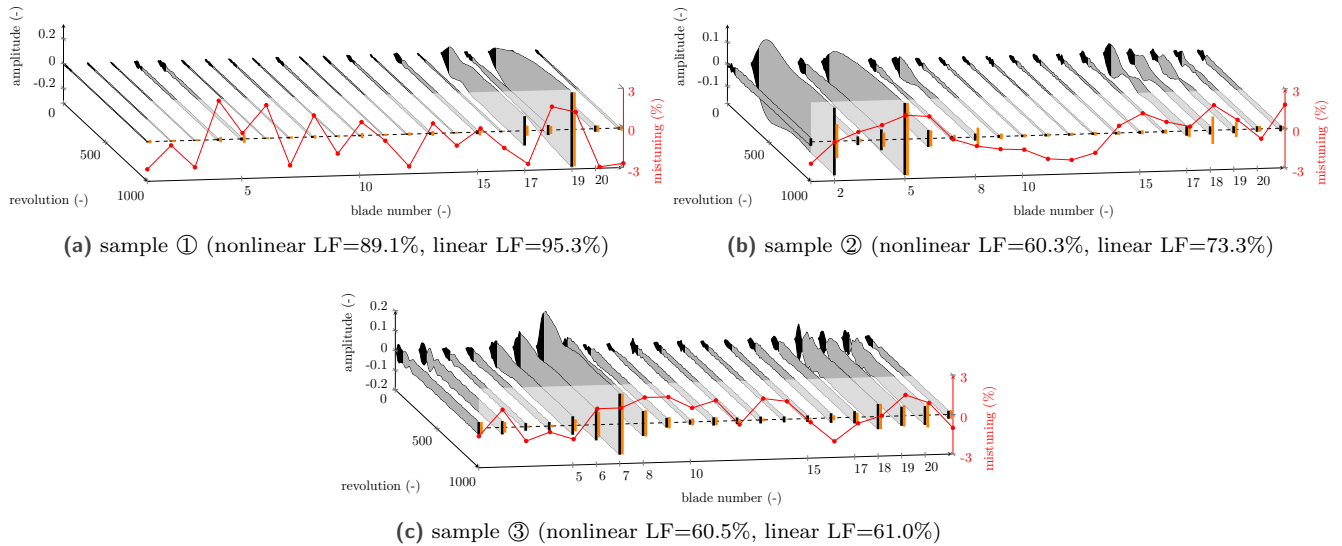


Figure 18. RADIAL DISPLACEMENTS AT THE LEADING EDGE OF EACH BLADE FOR CONTACT SIMULATIONS AFTER 1000 REVOLUTIONS (—) AND LINEAR VALUES (—)

CONCLUSION

This work proposed an analysis of the effect of small mistuning on rotor/stator interactions. After a detailed study of the tuned bladed disk dynamics in the case of an interaction between the first bending modes and the engine order 2, a stochastic analysis on the robustness of the interaction with respect to the mistuning levels has been undertaken. Different observations have emerged, and the results have been compared with those obtained with a linear forcing (without contact nonlinearities). First, an enlargement of the angular speed range on which the resonance occurs is observed in the nonlinear case compared to its linear counterparts. Secondly, nonlinear and linear amplification factors are of the same order of magnitude. This could be explained by the low contact stiffening of the studied configuration. The comparison between the linear and nonlinear amplification factor for each sample also highlights that no correlation exists between a mistuning pattern leading to high amplifications in a linear context or when contact nonlinearities are taken into account. Therefore, dedicated analyses on the effect of mistuning should be undertaken with contact nonlinearities considerations at the design stage especially if intentional mistuning is considered. Finally, lower localization factors are observed in the nonlinear case. Indeed, the diverging amplitude of vibration for different blades in nonlinear simulations during the transient motion leads to a lower localization of the vibration among the blades. Closer values are obtained considering the steady state solution.

Acknowledgments

This research was undertaken thanks to funding from the Natural Sciences and Engineering Research Council of Canada and the Canada Research Chairs Program.

References

- [1] Castanier, M. P., and Pierre, C., 2006. “Modeling and analysis of mistuned bladed disk vibration: Status and emerging directions”. *Journal of Propulsion and Power*, **22**, pp. 384–396. doi: 10.2514/1.16345.
- [2] Yuan, J., Scarpa, F., Allegri, G., Titurus, B., Patsias, S., and Rajasekaran, R., 2017. “Efficient computational techniques for mistuning analysis of bladed discs: A review”. *Mechanical Systems and Signal Processing*, **87**, pp. 71 – 90. doi: 10.1016/j.ymssp.2016.09.041.

- [3] Ewins, D. J., 1969. “The effects of detuning upon the forced vibrations of bladed disks”. *Journal of Sound and Vibration*, **9**(1), pp. 65–79. doi: 10.1016/0022-460X(69)90264-8.
- [4] Dye, R. C. F., and Henry, T. A., 1969. “Vibration Amplitudes of Compressor Blades Resulting From Scatter in Blade Natural Frequencies”. *Journal of Engineering for Power*, **91**(3), pp. 182–187. doi: 10.1115/1.3574726.
- [5] Pierre, C., and Cha, P. D., 1989. “Strong Mode Localization in Nearly Periodic Disordered Structures”. *AIAA Journal*, **27**(2), pp. 227–241. doi: 10.2514/3.10085.
- [6] Whitehead, D. S., 1976. “Research note: Effect of mistuning on forced vibration of blades with mechanical coupling”. *Journal Mechanical Engineering Science*, **18**(6), pp. 306–307. doi: 10.1243/JMES_JOUR_1976_018_049_02.
- [7] Martel, C., and Corral, R., 2009. “Asymptotic Description of Maximum Mistuning Amplification of Bladed Disk Forced Response”. *Journal of Engineering for Gas Turbines and Power*, **131**(2), p. 022506. doi: 10.1115/1.2968868.
- [8] Petrov, E., and Ewins, D. J., 2005. “Method for analysis of nonlinear multiharmonic vibrations of mistuned bladed disks with scatter of contact interface characteristics”. *Journal of Turbomachinery*, **127**, pp. 128–136. doi: 10.1115/1.1812781.
- [9] Panning, L., Sextro, W., and Popp, K., 2007. “Spatial dynamics of tuned and mistuned bladed disks with cylindrical and wedge-shaped friction dampers”. *International Journal of Rotating Machinery*, **9**, pp. 219–228. doi: 10.1155/S1023621X03000198.
- [10] Mitra, M., Zucca, S., and Epureanu, B. I., 2016. “Effects of contact mistuning on shrouded blisk dynamics”. In Proceedings of ASME Turbo Expo 2016, Turbomachinery technical conference and exposition. doi: 10.1115/GT2016-57812.
- [11] Joannin, C., Chouvier, B., Thouverez, F., Ousty, J.-P., and Mbaye, M., 2017. “A nonlinear component mode synthesis method for the computation of steady-state vibrations in nonconservative systems”. *Mechanical Systems and Signal Processing*, **83**, pp. 75 – 92. doi: 10.1016/j.ymsp.2016.05.044 - oai: hal-01389699.
- [12] Tang, W., and Epureanu, B. I., 2017. “Nonlinear dynamics of mistuned bladed disks with ring dampers”. *International Journal of Non-Linear Mechanics*, **97**, pp. 30 – 40. doi: 10.1016/j.ijnonlinmec.2017.08.001.
- [13] Pourkiaee, M., and Zucca, S., 2018. “Reduced order model for nonlinear dynamics of mistuned bladed disks with shroud friction contacts”. *Journal of Engineering for Gas Turbines and Power*, **141**, p. 011031. doi: 10.1115/GT2018-75223.
- [14] Zhao, W., Zhang, D., and Xie, Y., 2019. “Vibration analysis of mistuned damped blades with nonlinear friction and contact”. *Journal of Low Frequency Noise, Vibration and Active Control*, **38**(3-4), pp. 1505–1521. doi: 10.1177/1461348419836352.
- [15] Batailly, A., Agrapart, Q., Millecamps, A., and Brunel, J.-F., 2016. “Experimental and numerical simulation of a rotor/stator interaction event localized on a single blade within an industrial high-pressure compressor”. *Journal of Sound and Vibration*, **375**, August, pp. 308–331. doi: 10.1016/j.jsv.2016.03.016 - oai: hal-01342401.
- [16] Joachim, J., Nyssen, F., and Batailly, A., 2020. “Numerical Investigation of a Mistuned Academic Bladed Disk Dynamics with Blade/Casing Contact”. *Journal of Engineering for Gas Turbines and Power*, July. doi: 10.1115/1.4047780 - oai: hal-02896893.
- [17] Carpenter, N., Taylor, R., and Katona, M., 1991. “Lagrange constraints for transient finite element surface contact”. *International Journal for Numerical Methods in Engineering*, **32**(1), July, pp. 103–128. doi: 10.1002/nme.1620320107 - oai: hal-01389918.
- [18] Legrand, M., Batailly, A., and Pierre, C., 2011. “Numerical investigation of abradable coating removal in aircraft engines through plastic constitutive law”. *Journal of Computational and Nonlinear Dynamics*, **7**(1), September. doi: 10.1115/1.4004951 - oai: hal-00627526.

- [19] Batailly, A., Meingast, M., and Legrand, M., 2015. “Unilateral contact induced blade/casing vibratory interactions in impellers: Analysis for rigid casings”. *Journal of Sound and Vibration*, **337**, February, pp. 244–262. doi: 10.1016/j.jsv.2014.10.010 - oai: hal-01120157.
- [20] Millecamps, A., Brunel, J.-F., Dufrenoy, P., Garcin, F., and Nucci, M., 2009. “Influence of thermal effects during blade-casing contact experiments”. In ASME 2009 International Design Engineering Technical Conferences and Computers and Information in Engineering Conference. doi: 10.1115/DETC2009-86842 - oai: hal-01223060.
- [21] Lim, S.-H., Bladh, R., Castanier, M. P., and Pierre, C., 2007. “Compact, generalized component mode mistuning representation for modeling bladed disk vibration”. *AIAA Journal*, **45**(9), September, pp. 2285–2298. doi: 10.2514/1.13172.
- [22] Joachim, J., 2020. “Développement de modèles numériques de roues aubagées désaccordées dans un contexte non-linéaire”. PhD Thesis, Polytechnique Montreal. oai: tel-02888893.
- [23] Klauke, T., Kühhorn, A., Beirow, B., and Golze, M., 2009. “Numerical investigations of localized vibrations of mistuned blade integrated disks (blisks)”. *Journal of Turbomachinery*, **131**(3), p. 031002. doi: 10.1115/1.2985074.